H2 storage in isostructural UiO-67 and UiO-66 MOFs

H_2 storage in isostructural UiO-67 and UiO-66 MOFs

Sachin Chavan, Jenny G. Vitillo, Diego Gianolio, Olena Zavorotynska, Bartolomeo Civalleri, Søren Jakobsen, Merete H. Nilsen, Loredana Valenzano, Carlo Lamberti, Karl Petter Lillerud, Silvia Bordiga

Phys. Chem. Chem. Phys., 2012, **14**, 1614–1626

DOI: **10.1039/c1cp23434j**

H_2 storage in isostructural UiO-67 and UiO-66 MOFs†

Sachin Chavan,[1] Jenny G. Vitillo,[1] Diego Gianolio,[1] Olena Zavorotynska,[1] Bartolomeo Civalleri,[1] Søren Jakobsen,[2] Merete H. Nilsen,[2] Loredana Valenzano,[3] Carlo Lamberti,[1*] Karl Petter Lillerud,[2] Silvia Bordiga[1]

[1] Department of Inorganic, Physical and Material Chemistry, NIS Centre of Excellence, and INSTM reference center, University of Turin, Via P. Giuria 7, I-10125 Torino, Italy
[2] inGAP centre of Research-based Innovation, Department of Chemistry, University of Oslo, Sem Saerlandsvei 26, N-0315 Oslo, Norway
[3] Department of Physics, Michigan Technological University, 1400 Townsend Dr, Houghton, MI 49931-1295, USA

Abstract

The recently discovered UiO-66/67/68 class of isostructural metallorganic frameworks (MOFs) [*J. Am. Chem. Soc*., 2008, **130**, 13850] has attracted great interest because of its remarkable stability at high temperatures, high pressures and in presence of different solvents acids and bases [Chem. *Mater*., 2011, **23**, 1700]. UiO-66 is obtained connecting $Zr_6O_4(OH)_4$ inorganic cornerstones with 1,4-benzene-dicarboxylate (BDC) as linker resulting in a cubic MOF, already been successfully reproduced in several laboratories. Here we report the first complete structural, vibrational and electronic characterization of the isostructural UiO-67 material, obtained using the longer 4,4′ biphenyl-dicarboxylate (BPDC) linker combining laboratory XRPD, Zr K-edge EXAFS, TGA, thermogravimetry, FTIR, UV-Vis studies. Comparison between experimental and periodic calculations performed at B3LYP level of theory allows a full understanding of the structural, vibrational and electronic properties of the material. Both materials have been tested for molecular hydrogen storage at high pressures and at liquid nitrogen temperature. In this regard, the use of a longer ligand has a double benefit as (i) it reduces the density of the material and (ii) it increases the Langmuir surface area from 1281 to 2483 $m^2 g^{-1}$ and the micropore volume from 0.43 to 0.85 $cm^3 g^{-1}$. As a consequence, the H_2 uptake at 38 bar and 77 K increases from 2.4 mass% for UiO-66 up to 4.6 mass% for the new UiO-67 material. This value is among the highest vales reported so far but is lower than those reported for MIL-101, IRMOF-20 and MOF-177 in similar pressure and temperature conditions (6.1, 6.2 and 7.0 mass%, respectively) [*J. Am. Chem. Soc*., 2006, **128**, 3494; *Angew. Chem.-Int. Edit*., 2008, **47**, 6766]. Nevertheless the great chemical and thermal stability of UiO-67 and the absence of Cr in its structure would make this material competitive.

1. Introduction

Metallorganic frameworks (MOFs), also known as coordination polymers, a new class of hybrid materials have attracted much interest in the scientific community.[1-21] The interest of the industrial community[22,23] started also growing up with a 5-10 year in time delay, basically driven by the rapidly increasing number of new MOFs showing a good framework stability upon desolvation and thermal treatments.[16,17,24-35]

Due to high porosity,[36] absence of dead volume and low density MOFs have gained popularity as adsorbents. MOFs are among the promising materials for non-dissociative hydrogen storage[10,18,37-55] which is an important research topic that could solve our energy and environmental crisis.[56-60] The facile synthesis of MOFs from the inorganic and organic building blocks and the modular nature of MOFs enable to access not only unlimited number of structure but also gives control over the pore size, shape and functionality. Indeed several MOFs have been tested for the hydrogen uptake and various strategies have been employed to improve the uptake, thermodynamic

† This work is dedicated to Cesare Pisani, suddenly disappeared few weeks ago, taken by his passion on our Alps. He has been a guide for us in science and life. We will never forget him.

* Corresponding authors: C. Lamberti Tel: +39011-6707841 Fax: +39011-6707855; E-mail: carlo.lamberti@unito.it

and kinetics of hydrogen adsorption.[18,48,50,61] It is well known that the hydrogen uptake shown by material is directly proportion to its surface area. Therefore, one of the strategies used to increase the H_2 uptake was the synthesis of isostructural MOFs with extended topology obtained by using longer organic spacer of same geometry as in prototype MOF.[2,62] MOFs synthesized under such principle have shown record break surface area and the hydrogen uptake above the DOE (Department of Energy USA) target (6 mass%),[50] although these interesting values have been all obtained at a low temperature as 77 K, not feasible on the economical point of view for a spread use of H_2 as fuel in automotive. At room temperature, in fact, the stored amounts are sensitively less than 1 mass% also at pressures of 200 bar, because of the low enthalpies of adsorption of H_2 in MOFs. This means that, although promising this class of materials still need of a real breakthrough before that its use in this field becomes practically feasible. Nevertheless, their large flexibility in design has allowed to obtain an impressive improvement in the stored amounts in less than 5 years, going from the 1.3 mass% of MOF-5[38] to the 10 mass% of COF-105.[63] However, at present none of the existing systems for hydrogen storage are able to satisfy all the DOE conditions. For what concerns hydrides, on the contrary, high temperatures are needed in order to obtain fast kinetics, especially in the discharging process.

Here we present the results of hydrogen adsorption on UiO-67 (UiO: University of Oslo) that is isostructural with the prototype UiO-66. UiO-66 is the zirconium and terephthalic acid based MOF using 1,4-benzene-dicarboxylate (BDC) as linker,[30] while UiO-67 is obtained with the longer 4,4′ biphenyl-dicarboxylate (BPDC) as linker, see Figure 1. The interest shown by several laboratories in UiO-66 is due to the fact that it is one of the most resistant MOFs in terms of both thermal and chemical stability.[30,64] Due to the rigidity of the framework several isostructural UiOs has been prepared and tasted for the stability and gas adsorption. As an example, Kandiah et al.[65] studied the thermal and chemical stabilities of isostructural UiO-66-X (X= NH_2, Br and NO_2), observed the lower stability of this analogue with respect to parent UiO-66. Conversely UiO-67 shows thermal and chemical stability similar to that of UiO-66 with doubled the surface area.

H_2 adsorption isotherms are supported by parallel variable temperature IR experiments investigating the interaction of H_2 with UiO-67 in both hydroxylated (with μ3-OH) and dehydroxylated forms. Variable temperature IR spectroscopy is the perfect tool to understand the hydrogen interaction with surface sites.[66-69] The knowledge of the interaction between surface sites and adsorbing hydrogen molecule will help to modify the property of surface in order enhance the binding of incoming molecule.

The structure stability upon thermal treatment of UiO-67 has been checked by XRPD, EXAFS and TG experiment, showing to be a good as that of UiO-66. Finally, the dehydroxylated form of UiO-67 has been investigated with periodic density functional theory (DFT) calculations employing the hybrid B3LYP[70,71] functional as implemented in the CRYSTAL program.[72,73] Comparison with EXAFS, IR and UV-Vis data indicates an excellent agreement between theoretical and experimental results, allowing a complete understanding of the structural, vibrational and electronic properties of this complex material.

2. Materials and Methods

2.1 Materials

2.1.1. UiO-67. 300 ml DMF was added to 2.3 g (10 mmol) $ZrCl_4$ in an oven-dried 500 ml round bottom flask. The smoking (HCl) mixture was stirred a few minutes to get all the $ZrCl_4$ in solution, then 2.4 g (10 mmol) Biphenyl-4,4′-dicarboxylic acid was added. After stirring for 10 min, 0.25 ml (14 mmol) H_2O was added and 50 ml DMF to wash down any solids on the sides of the flask. The resulting white mixture was heated without stirring on an oil bath at 95°C for 100 h, cooled to RT and carefully filtered. Identification by PXRD. Yield: 4.4 g of white solid still containing some solvent in its cavities evaluated by TGA and BET preparation to app. 50 mass % bringing the yield of pure emptied sample to app. 2.2 g (ca. 63 %). The material was dried in vacuo 20 h to get an air and moisture stable sample. The total absence in the IR spectrum of the desolvated sample (vide

infra blue curve in Figure 5) of a component around $\nu = 1700$ cm^{-1}, fingerprint of the ν(C=O) mode, excludes the presence of any residual unreacted free acidic molecules.

2.1.2. UiO-66. For comparison, structural and H_2-adsorption properties of UiO-67 are compared to those obtained on isostructural UiO-66 MOF, that has already been successfully synthesized and functionalized in many laboratories worldwide. The synthesis of UiO-66 has already been detailed elsewhere.[30,74]

2.2 Experimental methods

2.2.1. XRPD. Powder X-ray Diffraction measurements were performed on a Bruker D5000 instrument with monochromatic CuKα1 radiation (λ = 1.540 Å) operated in Bragg-Bretano geometry and a variable slit. The instrument was equipped with a sample changer for PXRD plates giving non-transmission PXRD diffractograms. All data were collected at an ambient temperature. As synthesized materials (hydroxylated forms) were measured in air, while desolvated materials (dehydroxylated forms) were measured inside sealed capillaries, after thermal activation at 400 °C to check the framework stability.

2.2.2. TGA. Thermo gravimetric analysis (TGA) was carried out in a 20 % mixture of oxygen in nitrogen using a Rheometric Scientific STA 1500 instrument with an adapted gas supply system. The approximate sample weight was 10 mg and the heating rate 5 °C/min.

2.2.3. MID-IR. Infrared spectroscopic measurements were performed on a thin self supporting wafer of the samples by using a homemade cryogenic cell,[67,75] that allowed us to perform (i) *in situ* sample activation; (ii) gas dosage and (iii) variable-temperature Infrared (VTIR) spectroscopy of adsorbed hydrogen while simultaneously recording temperature and equilibrium pressure. Transmission FT-IR spectra were recorded at 1 cm^{-1} resolution using a MCT detector equipped Bruker Equinox-55 FTIR spectrometer of which sample compartment was modified to accommodate the cryogenic IR cell.

2.2.4. ATR. Vibrational framework modes have been collected in attenuated total reflection (ATR) mode on a Bruker single reflection ALPHA-Platinum ATR spectrometer with a diamond crystal. The instrument is located inside a glove box allowing spectra collection of activated samples in inert atmosphere.

2.2.5. DR-UV-vis-NIR. Electronic transitions have been measured on a Varian Cary 5000 spectrometer equipped with a reflectance sphere on thick self-supported pellets.

Volumetric measurements Surface area, pore volume and pore size distribution were obtained by N_2 adsorption measurements carried out at 77 K on a Micromeritics ASAP 2020 sorption analyzer.

2.2.6. H_2-uptake. Excess H_2 adsorption isotherms at 77 K were obtained over the 0 – 80 bar pressure range by volumetric analysis (PCI instrument by Advanced Materials Corporation, Pittsburgh PA). Ultra pure 6.0 grade H_2 (99.9999%V; Rivoira) was used. The activated powder (about 500 mg) was then transferred under nitrogen atmosphere in the measurement cell. The skeletal sample density of the samples was determined by helium isotherms conducted on the samples at 293 K in the 0-20 bar range by means of an intelligent gravimetric analyzer (IGA-002, supplied by Hiden Analytical Ltd, UK).

2.2.7. EXAFS. Extended X-ray absorption fine structure spectroscopy (EXAFS) on desolvated UiO-67 has been collected in transmission mode at the BM01B (SNBL) beamline of the ESRF. The white beam was monochromatized using a Si(111) double crystal; harmonic rejection was performed by using two flat mirrors. EXAFS spectra were collected in transmission mode. up to 20 Å^{-1} with a variable sampling step in energy, resulting in $\Delta k = 0.05$ Å^{-1}, and an integration time that linearly increases with k from 2 to 5 s/point to account for the low signal-to-noise ratio at high k values. Ionization chambers measuring I_0 and I_1 were optimized to have, at 18 keV, an absorption efficiency of 15 and 50%, respectively. UiO-67, in form of self supported pellets of optimized thickness, was located inside an *ad hoc* conceived cell[76] and measured in its desolvated form.

The extraction of the $\chi(k)$ function was performed using the Athena code.[77] For each sample, three consecutive EXAFS spectra were collected and corresponding $\chi(k)$ functions were averaged before data analysis.[78] EXAFS data analysis was performed using the Arthemis software.[77] Phase and amplitudes for all single scattering (SS) and multiple scattering (MS) paths were calculated by FEFF6 code[79] using as input the structure of the dehydroxylated UiO-66 solved by EXAFS in previous works,[30,74] The averaged k^3 $\chi(k)$ function was Fourier Transformed in the Δk = 2.00-15.00 $Å^{-1}$ interval. The fits were performed in R-space in the ΔR = 1.00-5.30 Å range ($2\Delta k\Delta R/\pi > 35$).

EXAFS spectra on UiO-66 have been collected in transmission mode at the BM29 beamline of the ESRF, as described in detail elsewhere,[30,74] and will be here used for comparison with the analogous data collected on UiO-66 to prove that both materials are constituted by the same Zr_6O_6 inorganic cornerstones.

2.2 Theoretical methods

The theoretical investigation of UiO-67 MOF (in its hydroxylated and dehydroxylated structures) was carried out with periodic density functional theory (DFT) calculations employing the hybrid B3LYP[70,71] functional as implemented in the CRYSTAL program.[72,73] Crystalline orbitals (CO) are represented as linear combinations of Bloch functions (BF), and are evaluated over a regular three-dimensional mesh in the reciprocal space. Each BF is built from local atomic orbitals (AO), which are contractions (linear combinations with constant coefficients) of Gaussian-type functions (GTFs), each GTF being the product of a Gaussian times a real solid spherical harmonic.

As already successfully done for the isostructural UiO-66,[74] the following computational details have been adopted. All electron basis sets were used for Zr, O, C and H atoms; they consist of (8*s*)-(7631*sp*)-(621*d*), (8*s*)-(411*sp*)-(1*d*), (6*s*)-(31*sp*)-(1*d*) and (31*s*)-(1*p*) respectively. Basis sets for Zr and O were taken from ref.[80] and ref.[81] whereas for C and H standard 6-311G(*d,p*) basis sets from Pople's family were adopted. Polarization functions (one shell) were used on H, C and O atoms. The corresponding exponents are: α(H, *p*) = 0.1; α(O, *d*) = 0.8, α(C, *d*) = 0.8. For Zr, an extra *d*-function was adopted with exponent α(Zr, *d*) = 0.4. The effect of a polarization *f* orbital (α=0.6) was investigated showing no significant improvement in the results. For the numerical integration of the exchange–correlation term, 75 radial points and 974 angular points (XLGRID) in a Lebedev scheme in the region of chemical interest were adopted. The condition for the SCF convergence was set to 10^{-8} and 10^{-10} Hartrees during geometry optimization and frequency calculation steps, respectively. The Pack-Monkhorst/Gilat shrinking factors for the reciprocal space were set to 2, corresponding to 3 real reciprocal space points at which the Hamiltonian matrix was diagonalized. The five truncation criteria (TOLINTEG) for the bielectronic integrals (Coulomb and HF exchange series) were set to 7 7 7 7 16.[73] A modified Broyden scheme[82] following the method proposed by Johnson[83] was adopted to accelerate convergence in the self-consistent calculations; the method was applied after five SCF iterations, with 50% of Fock/KS matrices mixing and with the Johnson parameter set to 0.05. The above computational parameters ensured a full numerical convergence on all the computed properties described in this work.

Both the hydroxylated and dehydroxylated structures were derived from the experimental geometry (cubic, space group *Fm-3m*, No. 225); the former was optimized in the space group *F*23 (cubic, No. 196) while the calculations on the latter were performed in the space group *R32* (trigonal, No. 155). A full relaxation of the structures (both lattice parameters and atomic positions) was performed by keeping the symmetry of the systems; optimizations were iterated until no changes appeared in the geometry.

The calculations of vibrational frequencies at the Γ point, were performed on the optimized geometry by means of a mass-weighed Hessian matrix obtained by numerical differentiation of the analytical first derivatives.[84,85] Full details and discussion of the computational conditions and other numerical aspects can be found elsewhere.[86]

3. Results and discussion

Since its discovery in late 2008,[30] UiO-66 has immediately been recognized by the scientific community as one of the most promising MOF materials for both catalytic and photocatalytic application and the synthesis of UiO-66 and of functionalized derivatives has been well documented in the literature coming from several laboratories.[11,12,64,65,87-101]

Conversely, to the best of our knowledge, only Schaate et al.[101] have so far been able to reproduce the synthesis of UiO-67. This material has consequently still to be considered as a prototype material, which synthesis and framework stability and properties have to be checked and confirmed by the scientific community. For this reason, before entering in the discussion of the interaction between H_2 and UiO-67 (Section 3.4), we report a detailed description of the structural (Section 3.1), vibrational (Section 3.2) and electronic (Section 3.3) properties of UiO-67 comparing experimental and theoretical results. Sections 3.1-3.3 represent the first complete characterization of UiO-67 and are the proofs that the H_2 adsorption data reported in Section 3.4 have been obtained on a material that actually corresponds to the target UiO-67.

3.1. Structural characterization

3.1.1. Description of the target UiO-66 and UiO-67 structures. Recent detailed study on the structural, vibrational and electronic properties of UiO-66 by Valenzano et al.[64] confirm that the inorganic brick in UiO-66 is consist of an $Zr_6O_4(OH)_4$ core in which the triangular faces of the Zr_6-octahedron are alternatively capped by μ3-O and μ3-OH groups. Upon thermal treatment at 300°C two H_2O molecule per $Zr_6O_4(OH)_4$ cluster leave the structure giving de-hydroxylated MOF in which inorganic cluster rearrange into distorted Zr_6O_6 cluster (vide infra the top inset in Figure 3).

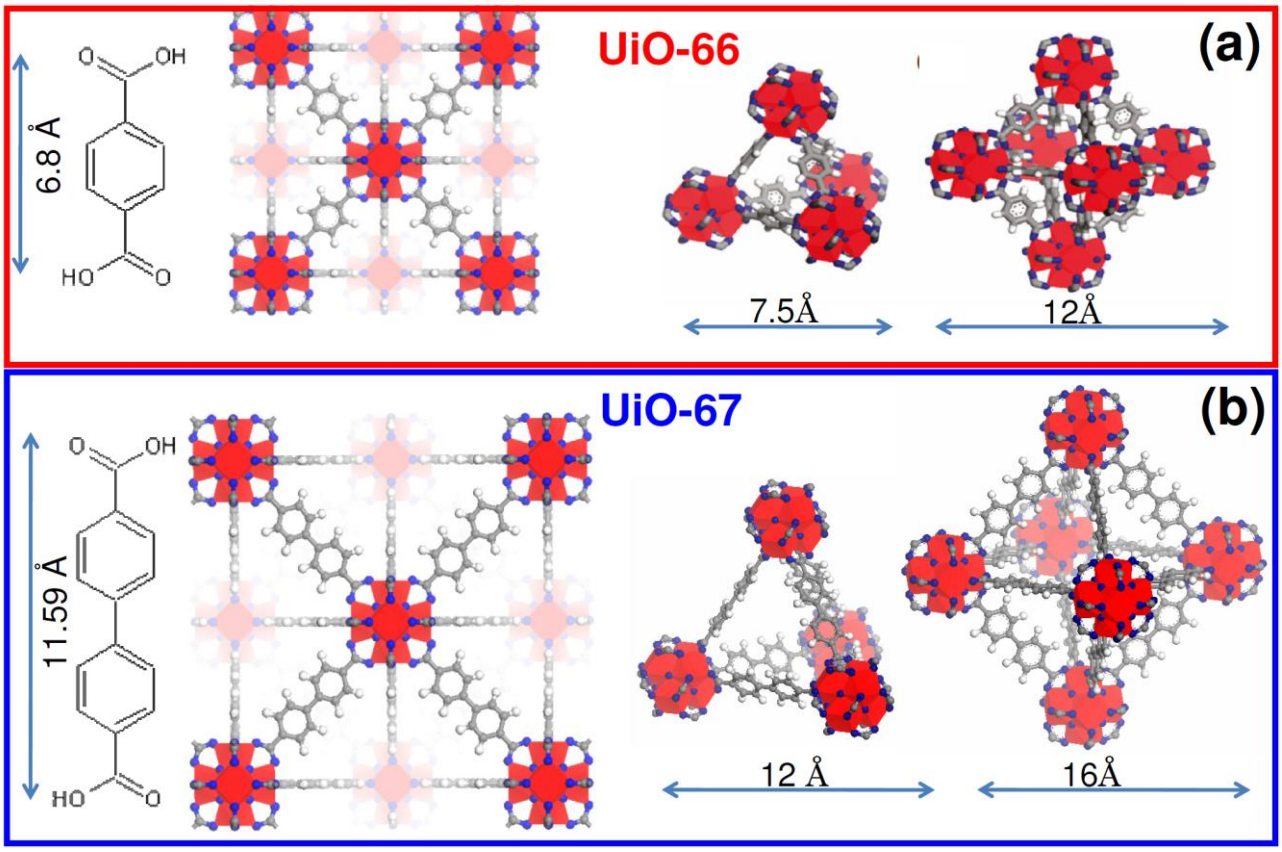

Figure 1. From left to right: comparison of the dimension of linker, structure, tetrahedral and octahedral cages (d) for the isostructural UiO-66 and UiO-67 MOFs, parts (a) and (b), respectively.

UiO-67 is 3D, porous and isostructural to the prototype UiO-66 Zr-MOF being the linker the only difference, see Figure 1.[30] The use of BPDC in stead of BDC ligand results in symmetric

expansion of UiO-66 topology. The inorganic brick in the structure, is still 12 coordinated $Zr_6O_4(OH)_4(CO_2)_{12}$ cluster that gives high temperature stability to both prototype UiO-66 and UiO-67 framework. The longer linker implies that both the tetrahedral and octahedral micro porous cages are of wider dimension in the UiO-67 case (Figure 1cd), moving from 7.5 to 12 Å and from 12 to 16 Å, respectively.

For H_2 storage purposes the use of a longer ligand has a double benefit. On one hand it implies a decrease of the sample density, on the other it allows larger internal empty volumes to host H_2 molecule in the liquid-like state, see right parts in Figure 1.

3.1.2 Frameworks stability and porosity: comparison among UiO-66 and UiO-67. The cages of as synthesized MOF are occupied by solvent molecules (DMF, H_2O); upon thermal treatment at appropriate temperature either to as synthesized or solvent exchanged material, de-solvated and de-hydroxylated form of the framework can be obtained. Similar to UiO-66, the UiO-67 framework is also very stable to high temperature treatment as evaluated by XRPD data collection (Figure 2a) and by thermo gravimetric (TG) analysis (Figure 2b).

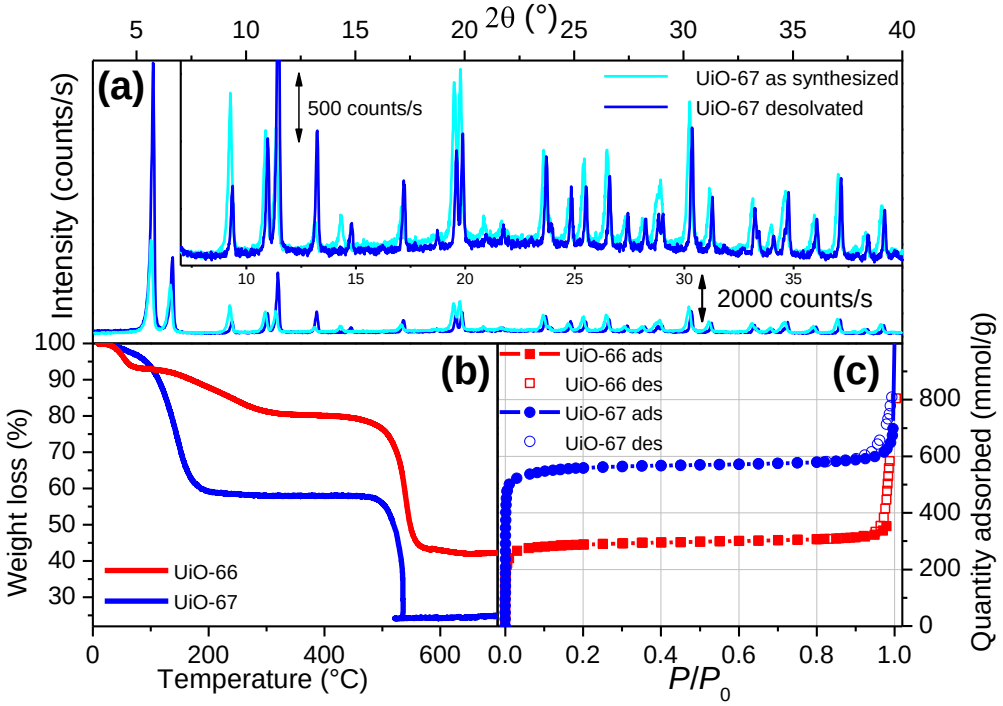

Figure 2. Part (a): Comparison of the XRPD pattern for UiO-67 as prepared (cyan curve) and activated at 300 °C (blue curve). The inset report a magnification of the high 2θ region. Part (b): TGA curve of UiO-67 and UiO-67 samples, red and blue curves, respectively. In both cases, the heating ramp was of 5 C/min in a N_2 flow (100ml/min). Part (c): volumetric N_2 adsorption isotherms recorded at 77 K on UiO-66 (red squares) and UiO-67 (blue circles). Empty and filled scatters refer to the adsorption and desorption branches, respectively.

As was the case for UiO-66,[30,64] solvent removal left the XRPD pattern of UiO-67 almost unchanged: all peaks are present at almost the same angular position, just characterized by a small intensity variation. The presence of the diagonal linkers combined with the strong linker-inorganic brick interaction is responsible for the high rigidity and an exceptional thermal and chemical stability of the framework. TG analysis of the UiO-67 (blue curve in Figure 2b) shows two steps weight loss prior to the formation of final ZrO_2 product. The first step of 42 % weight loss (20-300°C), is assigned to the loss of solvent. This value is more then the double then the corresponding weight loss observed for UiO-66 (red curve in Figure 2b) and is a consequence of the larger internal volume of UiO-67. The blue curve shows a stability plateau in the range of 300-500°C range before a second step of additional 34% weight loss(500-560°C), corresponds to the thermal decomposition of solid occur and the formation of ZrO_2. This second step exhibits a larger weight loss than that

observed for UiO-66 because of higher relative mass of the ligand. From this weight loss we obtain the ratio between Zr and linker masses, that is 1:1.4 for UiO-67 and ranges between 1:0.9 and 1:1.1 for UiO-66. In both cases a bit less than expected from the theoretical stoichiometric composition, probably due to some missing linkers.[64]

The stability of the framework after the treatment at 300°C was also confirmed by the surface area measurements (see Table 1). The N_2 isotherms are of Type Ib (see blue curve Figure 2c), indication of a perfectly micro porous material possessing a very narrow pore size distribution. The shape of the N_2 isotherms is the same reported for UiO-66, with the plateau shifted at higher adsorbed volume. Accordingly, the UiO-67 surface area (S_{BET} = 1877 m^2 g^{-1}) and micro pore volume (V_{micro} = 0.85 cm^3 g^{-1}) are more than the double than those of UiO-66 (S_{BET} = 850 m^2 g^{-1} and V_{micro} = 0.43 cm^3 g^{-1}), as expected. Table 1 summarizes the results of the BET analysis on both materials. As far as UiO-67 is concerned, the disagreement between $S_{Langmuir}$ and S_{theor} is in the order of 10% (see Table 1), a value that is in line with the results obtained on this class of materials. Many washing/activation methods has been tested for UiO-67: washing with DMF, MeOH, EtOH, Ether, boiling in water and just heating to 250-300 °C, without altering the observed surface area.

Table 1. Surface area (m^2 g^{-1}) and pore volume (cm^3 g^{-1}) of UiO-66 and UiO-67.

Sample	S_{BET} [a]	$S_{Langmuir}$ [a]	S_{theor} [b]	S_{micro} [a]	V_{tot} [c]	V_{micro} [d]
UiO-66	969	1281	974	925	0.52	0.43
UiO-67	1877	2483	2850	2443	0.95	0.85

[a] Total area evaluated following the BET and Langmuir model in the standard $0.05 < P/P_0 < 0.25$ pressure range.
[b] Calculated by using a GCMC method (probe radius = 1.82 Å).
[c] Total pore volume calculated as volume of the liquid at $p/p_0 \approx 0.97$.
[d] Micropore volume and surface area obtained from the t-plot by using the Harkins and Jura equation.

3.1.3. EXAFS refinement: comparison between UiO-66 and UiO-67. Being EXAFS an atomically selective technique,[102] Zr K-edge EXAFS on iso-reticular UiO-66 and UiO-67 will inform on the structure of the respective Zr_6O_6 inorganic cornerstone only. We are consequently expecting to obtain basically the same result on the two compounds. Indeed, the local nature of the technique will prevent EXAFS to appreciate the change of the ligand from BDC to BPDC. Notwithstanding this limitation the technique will have as major goal to testify that the two materials have the same inorganic cornerstone. Secondarily, we will learn from EXAFS if the two different ligands have some effect in determining small structural changes in the Zr_6O_6 structure. It is indeed well known from literature that EXAFS spectroscopy has been of great help in elucidating the local structure of inorganic cornerstones[14,27-30,64,92,103,104] or of inorganic backbone[14,105-108] for different MOFs materials.

Figure 3 reports a direct comparison between the EXAFS spectra of the dehydroxylated forms of UiO-66 (red curves) and UiO-67 (blue curves) in both k and R spaces. Form a simple view on the experimental data it is evident that data collected on UiO-66 and UiO-67 are, as expected, very similar. In k-space (inset in Figure 3) only a small shift in the maxima and minima of the $k^3\chi(k)$ is appreciable in the low k region. This is simply due to the different extraction procedure adopted for treating two data collected on two different beamlines, particularly the E_0 definition. This discrepancy will be cured in the EXAFS data analysis by optimizing the parameter ΔE, see Table 2. Also in R-space the two data are very similar. UiO-67 results in slightly less intense signals. This effect could be related either to an increase degree of heterogeneity or to a small variation in the bond length resulting in a more destructive interference among the different single scattering (SS) and multiple scattering (MS) paths. To discriminate among these two possibilities, a detailed EXAFS data analysis must be carried out.

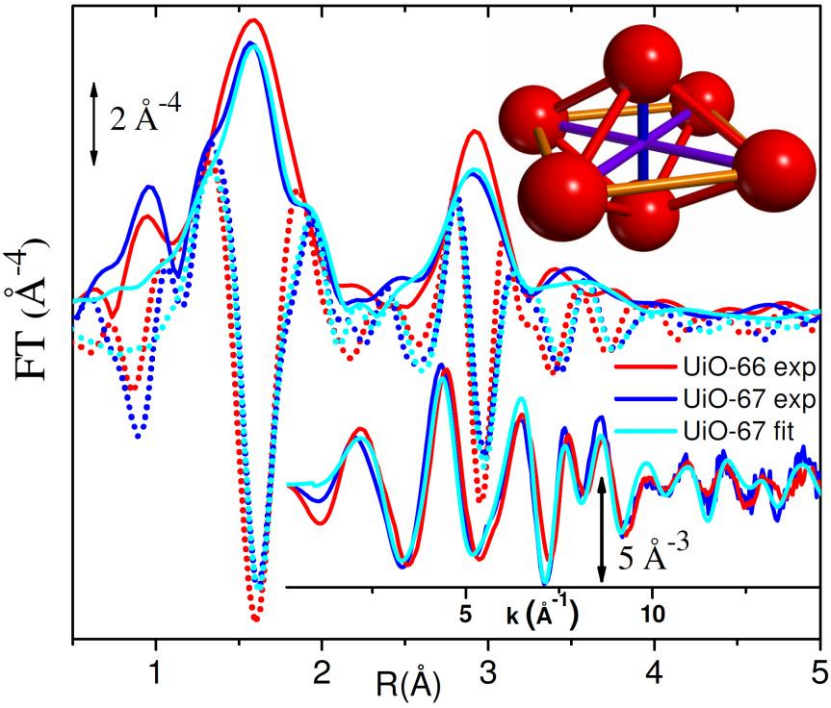

Figure 3. Direct comparison of the k^3-weighted, phase uncorrected, FT of the EXAFS spectra collected on UiO-66 (ESRF, BM29, red curves) and UiO-67 (ESRF, BM01A, blue curves) in their dehydroxylated forms. Also reported is the best fit performed on UiO-67 sample (cyan curve). Full and dotted lines refer to the modulus and the imaginary parts, respectively. The bottom inset reports the same data in k-space. The top inset reports the scheme of the distorted Zr_6O_6 inorganic cornerstone: only Zr atoms are shown as red spheres, while O atoms are omitted for clarity. The 12 sides and the 3 diagonals of the octahedron results in the R_{Zr1} and R_{Zr2} distances measured by EXAFS. For a perfect octahedron the 12 R_{Zr1} and the 3 R_{Zr2} are equivalent. The squeezing of the two apical Zr atoms results in 8 (out of 12) short R_{Zr1a} distances (red bars, linking one apical and one planar Zr atom) and 4 (out of 12) long R_{Zr1b} distances (orange bars, linking two planar Zr atoms). For the diagonal, the squeezing results in 1 (out of 3) short R_{Zr2a} distance (blue bar, linking the two apical Zr atoms) and 2 (out of 3) long R_{Zr2b} distances (violet bars, linking the 2 couples of opposite planar Zr atoms).

The closer resemblance between the experimental data colleted on the dehydroxylated forms of UiO-66 and UiO-67 (Figure 3), allows us to adopt for UiO-67 the same refinement procedure adopted to solve the structure of dehydroxylated UiO-66.[64] Results are summarized in Table 2 and Figure 3 (Blue and cyan curves). The model foreseen that the perfect $Zr_6(OH)_4O_4$ octahedron forming the cornerstone of the as synthesized material evolves along the dehydroxylation process in to a distorted Zr_6O_6 octahedron where both the Zr-Zr distances of the side (R_{Zr1}) and of the diagonal (R_{Zr2}) of the octahedron are split into a long and a short couple of distance labeled as (R_{Zr1a}, R_{Zr1b}) and (R_{Zr2a}, R_{Zr2b}), respectively. The distortion is depicted in the top inset of Figure 3.

The strong intensities of the Zr1a and Zr1b signals allow to determine the corresponding contributions in R-space just by looking to the modulus of the Fourier Transform (FT) of the experimental EXAFS spectrum. Zr2a and Zr2b signals are much less intense because both of their longer distance from the absorber and their low coordination numbers (N_{Zr1a} = 1/3; N_{Zr1a} = 2/3, see Table 2) and their location can not be appreciated from the modulus, but it can be guessed looking to the imaginary part of the FT. To obtain precise Zr-O and Zr-Zr distances a fit of the EXAFS spectrum has to be performed. The fit locates the Zr2a contribution at 4.15 ± 0.07 Å, i.e. basically the same value found in the UiO-66 case[64] (4.14 ± 0.07 Å, see Table 2). The optimized value of R_{Zr2b} = 5.30 ± 0.04 Å well agrees with the value predicted by the simple apical squeezed model ($R_{Zr2b} = \sqrt{2}\ R_{Zr1b}$ = 5.37 Å). Please note also that the distance of R_{Zr2a} = 4.15 ± 0.07 Å well agrees with the model of an apical-squeezed octahedron, predicting $R_{Zr2a} = \sqrt{[4\ R^2_{Zr1b} - R^2_{Zr2b}]}$ = 4.07 Å.[64]

Coming to the two first shell Zr-O distances, both are significantly stretched with respect to those measured for the UiO-66 material. The μ3-O are located at $R_{\mu3\text{-}O}$ = 2.096 ± 0.007 Å, with a variation of $\Delta R_{\mu3\text{-}O}$ = +0.04 ± 0.01 Å), while the average of the longer distances is optimized at

R_{O1}= 2.249 ± 0.007 Å: ΔR_{O1} = 0.03± 0.01 Å. Within the experimental errors the distance R_C to the four carbon atoms of the linkers is the same as found for UiO-66 but, as clearly underlined in the previous works[64] this distance refined by EXAFS is not reliable as superimposed with four MS paths, two of them of higher strength. The shortest octahedron side R_{Zr1a} (3.35 ± 0.01 Å and 3.36 ± 0.01 Å) and the shortest diagonal R_{Zr2a} (4.14 ± 0.07 Å and 4.15 ± 0.07 Å) are comparable in both UiO-66 and UiO-67, respectively. the longer octahedron side R_{Zr1d} and the longer diagonal R_{Zr2b} (3.80 ± 0.03 Å and 5.46 ± 0.05 Å) of uiO-67 are conversely slightly stretched with respect to the UiO-66 case (3.74 ± 0.02 Å and 5.30 ± 0.04 Å). The differences observed for the R_{Zr2b} distances has to be considered with care, because of the large associated error bars, while the difference in the R_{Zr1b} distances is more solid.

Table 2. Summary of the EXAFS refinement obtained on the dehydroxylated forms of UiO-66 and UiO-67 (Δk = 2.0-15.0 Å^{-1}; ΔR = 1.0-5.3 Å,. EXAFS refinement was obtained using as input model the optimized structure from *ab initio* calculations. With this approach the coordination number (N) of each contribution is fixed by the model stoichiometry; such values are reported for each shell in parenthesis. Refinement of the experimental amplitude is done by optimizing the overall amplitude factor S_0^2 only. The fitting of the higher shells was possible only adopting the axial compressed model of the Zr_6O_6 octahedron represented where eight octahedron sides R_{Zr1} are split into eight short prismatic distances (R_{Zr1a}, N=8/3) and four long planar ones (R_{Zr1b}, N=4/3) and where the three diagonals R_{Zr2} are split into a short axial diagonal and (R_{Zr2a}, involving two Zr atoms out of six; N=1/3) and two long planar diagonals (R_{Zr2b}, involving four Zr atoms out of six; N=2/3).

	Dehydroxylated UiO-66	Dehydroxylated UiO-67
Ref.	[64]	This work
R-factor	0.02	0.04
Δk (Å^{-1})	2.0-15.0	2.0-15.0
ΔR (Å)	1.0-5.3	1.0-5.3
Ind points	35	35
N. variables	15	15
ΔE_0 (eV)	5	1
S_0^2	1.17	1.17
$R_{\mu 3\text{-}O}$ (Å)	2.06 ± 0.01 (N = 2)	2.096 ± 0.007 (N = 2)
$\sigma^2(\mu_3\text{-}O)$ (Å^2)	0.008 ± 0.003	0.006 ± 0.001
R_{O1} (Å)	2.221 ± 0.007 (N = 5)	2.249 ± 0.007 (N = 5)
σ^2(O1) (Å^2)	0.007 ± 0.002	0.004 ± 0.001
R_C (Å)	3.17 ± 0.04 (N = 4)	3.15 ± 0.04 (N = 4)
σ^2(C) (Å^2)	0.009 ± 0.009	0.004 ± 0.003
R_{Zr1a} (Å)	3.35 ± 0.01 (N = 8/3)	3.365 ± 0.015 (N = 8/3)
σ^2(Zr1) (Å^2)	0.009 ± 0.001	0.009 ± 0.002
R_{Zr1b} (Å)	3.74 ± 0.02 (N = 4/3)	3.80 ± 0.03 (N = 4/3)
σ^2(Zr1b) (Å^2)	0.009 ± 0.002	0.008 ± 0.003
R_{Zr2a} (Å)	4.14 ± 0.07 (N = 1/3)	4.15 ± 0.07 (N = 1/3)
σ^2(Zr2) (Å^2)	0.008 ± 0.006	0.006 ± 0.004
R_{Zr2b} (Å)	5.30 ± 0.04 (N = 2/3)	5.46 ± 0.05 (N = 2/3)
σ^2(Zr2b) (Å^2)	0.008	0.006
α	0.00 ± 0.01	0.01 ± 0.01
σ^2 (global) (Å^2)	0.007 ± 0.003	0.006 ± 0.004
Highest correlations	$\sigma^2(\mu_3\text{-}O)/\sigma^2(O1)$ = 0.78 $\sigma^2(O1)/R_{\mu 3\text{-}O}$ = 0.76 $R_{O1}/\sigma^2(\mu_3\text{-}O)$ = -0.63 |remaining| < 0.56	$\sigma^2(Zr1) / R_C$ = 0.855 $R_{Zr1} / \sigma^2(C)$ = -0.71 $R_{O1}/ R_{\mu 3\text{-}O}$ = 0.62 $\sigma^2(\mu_3\text{-}O)/\sigma^2(O1)$ = 0.61 |remaining| < 0.49

Summarizing, EXAFS confirms that the inorganic cornerstone of UiO-67 is the distorted Zr_6O_6, as is the case for UiO-66, and has been able to appreciate some minor distortions due to the use of two different ligands.

3.1.4. Theoretical periodic calculations. Here we report a periodic *ab initio* DFT (at the B3LYP level of theory) computational study carried out by using the CRYSTAL code[72,73] on UiO-67 material in both its hydroxylated and dehydroxylated forms. This code was already successfully applied to the study of other MOFs materials such as UiO-66,[64] MOF-5,[109] Cr-MIL-53,[110] Al-MIL-53,[111] CPO-27-Mg[74] and CPO-27-Ni.[108]

Table 3 reports the summary of the most relevant distances in the hydroxylated and dehydroxylated forms of UiO-67 as optimized at the periodic P3LYP level of theory. In the structure of UiO-67, the linker twists with respect to the center: i.e. the two phenyl groups twist with opposite angle with respect to the cavity. This reduces the symmetry of the structure; from space group [*F*-43*m* (216)], used for the UiO-66 structure,[74] down to the space group [*F*23 (196)], still cubic, though. This causes a splitting of the R_{O1} and of the R_C distances between Zr atoms and the O and C atoms of the linker, due to the presence of two crystallographic independent O and C atoms of the linker in *F*23 space group. Table 3 also reports the average values of such distances. Beside this aspect, the structure of the $Zr_6O_4(OH)_4$ inorganic cornerstones, in terns of relative distances among atoms, is virtually the same for the hydroxylated forms of UiO-67 and UiO-66 homologues.

The same holds for the Zr_6O_6 inorganic cornerstones of the dehydroxylated form (right part in Table 3) that exhibit very similar distances to those obtained in the calculations on the UiO-66 homologue at the same level of theory.[64] In the present case the dehydroxylated form of UiO-67 has been optimized in the [*R*32 (155)] space group.

Table 3. Comparison of the hydroxylated (left) and dehydroxylated (right) forms of UiO-67 structures as refined from periodic B3LYP approach. Listed in order of increasing distances from the Zr0 atom (acting as absorber for EXAFS), are reported: the type of neighbor, the degeneration (D), the single (R) and the averaged (<R>) distances.

neighbor	Hydroxylated form Periodic B3LYP *F*23 (196)			neighbor	Deydroxylated form Periodic B3LYP *R*32 (155)		
	D	R (Å)	<R> (Å)		D	R (Å)	<R> (Å)
μ_3-O	2	2.089	2.089	μ_3-Oa	1	2.054	2.056
				μ_3-Ob	1	2.058	
O1	2	2.253	2.249	O1a	1	2.201	
O1’	2	2.244		O1b	1	2.201	
μ_3-OH	2	2.285		O1c	1	2.226	2.222
				μ3-Oc	1	2.236	
				O1d	1	2.244	
C1	2	3.258	3.266	C1a	1	3.211	
C1’	2	3.274		C1b	1	3.216	3.238
				C1c	1	3.223	
				C1d	1	3.302	
Zr1	4	3.570	3.570	Zr1a	2	3.462	3.599
				Zr1b	2	3.735	
Zr2	1	5.049	5.049	Zr2	1	5.090	5.090

The agreement between periodic B3LYP calculations and EXAFS is quite good as can be observed comparing the results reported in Table 2 and Table 3. The following differences have been obtained between theoretical and experimental distances: $\Delta R_{\mu 3\text{-}O}$ = -0.04 Å; ΔR_{O1} = -0.027 Å; ΔR_C = +0.088 Å; ΔR_{Zr1a} = +0.097 Å; ΔR_{Zr1a} = -0.065 Å.

3.2. Vibrational properties of hydroxylated and dehydroxylated UiO-67

3.2.1. ATR vs. theoretical calculations. Figure 4 reports a direct comparison between experimental (top) and theoretical (bottom) framework modes of UiO-67 in its hydroxylated (cyan spectra) and dehydroxylated (blue spectra) forms. Experimental and computed spectra are in very good

agreement thus allowing an assignment of the main observed IR peaks. Actually, as the vibrational modes of UiO-67 are very close to those of the UiO-66 homologue, compare the cyan-blue spectra with the orange-red ones in the bottom part of Figure 4. This fact allows a straightforward assignment of the main framework modes of UiO-67 on the basis of the deep discussion presented elsewhere on the UiO-66 homologue.[64]

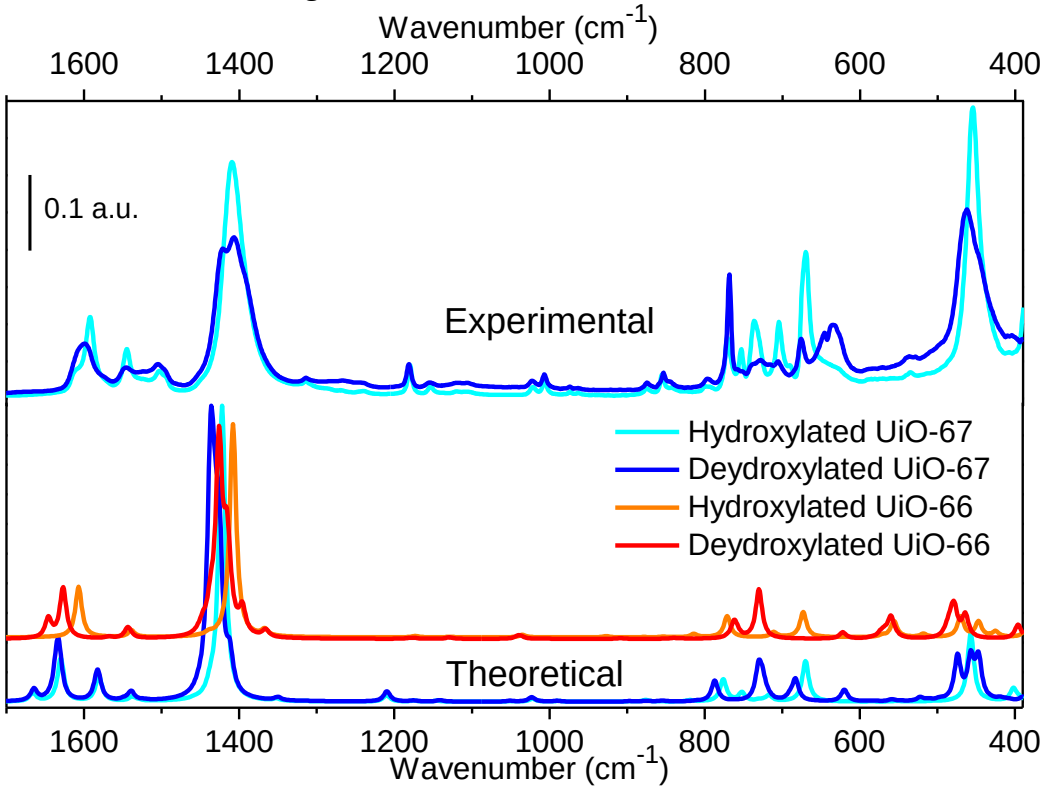

Figure 4. Vibrational framework modes of UiO-67 in its hydroxylated (cyan curves) and dehydroxylated (blue curves) forms. Top: experimental ATR IR spectra. Bottom: Theoretical spectra computed at the Γ point, on the optimized geometries, by means of a mass-weighed Hessian matrix obtained by numerical differentiation of the analytical first derivatives.[84,85] No scaling factor has been applied to the theoretical curves.

In this context we can consequently be very short, reporting in Table 4 a selection of the calculated vibrational frequencies (and the description of the corresponding normal modes) for UiO-67 and UiO-66 in both their hydroxylated and dehydroxylated forms. The only relevant difference is due to the band at 1210 cm^{-1} (1180 cm^{-1} in the experimental spectra) that is observed on UiO-67 only. This band is due to collective modes of the BPDC linker mainly involving bending modes of the hydrogen atoms of the rings. In both theoretical and experimental spectra, this band is almost unaffected by the dehydroxylation process as the inorganic cornerstones does not participate to the modes. Modes animation can be visualized at the CRYSTAL web-page.[112]

Table 4. Selection of calculated harmonic vibrational modes (in cm^{-1}) compared for the two structures. See the bottom part of Figure 4 for a graphical representation of the calculated spectra. No scaling factor has been adopted. Refer to the CRYSTAL web-page[112] for the full calculated spectra.

UiO-67		UiO-66		
Hydroxylated	Dehydroxylated	Hydroxylated	Dehydroxylated	Description of the mode
This work	This work	Ref. [64]	Ref. [64]	
1630, 1667	1634, 1665	1607	1568, 1627, 1648	OCO asymmetric stretching (in-phase/anti-phase)
1538	1540	1539	1541, 1545	CC ring
1422	1425, 1436	1408	1412, 1426	OCO symmetric stretching
1352	1350	1367	1364, 1367	CC ring
1210	1209	-	-	collective mode of the BPDC linker
819	-	814	-	OH bending + CH bending (anti-phase)
776	787	771	762	OH bending + CH bending (in-phase)
717	-	711	-	OH bending + CC ring + OCO bending
670	730	673	730	μ_3-O stretching
-	620	-	622	Zr-(OC) symmetric stretching
552	559	556	560	Zr-(OC) asymmetric stretching
-	522	518	-	out-of-plane ring deformation
457	-	470	-	μ_3-OH stretching (in-phase)
-	474, 457, 448	-	478, 464	out-of-plane ring deformation
-	-	447	-	μ_3-OH stretching (anti-phase)
402	-	425	-	μ_3-OH stretching

3.2.1 Transmission FTIR spectroscopy. The detail assignment for the all vibrations of UiO-66 framework is given elsewhere.[74] Therefore only the vibrations which undergoes in change upon de-solvation are discussed here for UiO-67. Figure 5 show the main spectral regions of the IR spectra of UiO-67, in which changes occur.

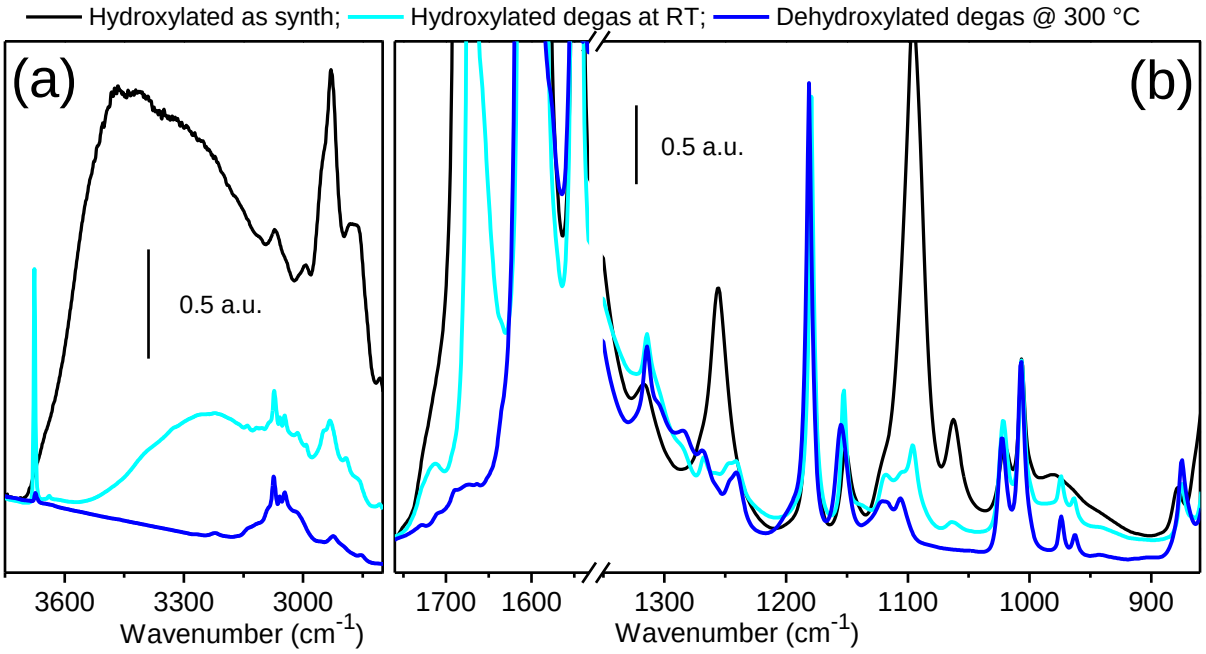

Figure 5. Effect of the desolvation on the FTIR spectra of UiO-67. Part (a) ν(OH) stretching region. Part (b) skeletal modes region. As prepared sample(black curve); sample degassed at room temperature, representing the hydroxylated form (cyan curve); sample degassed at 300°C for 30 min, representing the dehydroxylated form (blue curve). a. u. = absorbance units.

The IR spectrum of the completely solvated (H_2O/DMF) UiO-67 (black curve in Figure 5a, b) in the high frequency region (3800-1500 cm^{-1}) is dominated by broad band centered at 3430 cm^{-1} and doublet at 2930 and 2873 cm^{-1}. These are assigned to the hydrogen-bonded adsorbed water and ν(C-H) stretching modes of the physisorbed DMF. In the low frequency region (Figure 5b) the absorption bands which undergo changes upon degassing are seen at: broad and intense absorption at 1662 cm^{-1}, medium intense band at 1256 cm^{-1} and intense sharp band at 1096 $cm^{-1}$with a shoulder at 1062 cm^{-1}. These bands are respectively assigned to the $\delta(OH_2)$, $\delta(CH_3)$ and ν(C-O) vibration of the physisorbed water and DMF.

The spectrum obtained upon degassing at room temperature illustrated by cyan curve Figure 5 relevant changes are seen in both frequency regions. In high frequency region(Figure 5a) the broad band at 3430 cm^{-1} and the doublet at 2930 -2873 cm^{-1} shows significant decrease in an intensity with a shift in maxima of first to 3240 cm^{-1} , is mainly due to removal of physisorbed solvent (H_2O and DMF). The growth of a sharp new component is observed at 3676 cm^{-1} and is assigned to the ν(O-H) stretching of μ_3-OH present at the Zr_6-octahedron. In the low frequency region 1256, 1096 and 1062 cm^{-1} bands associated to solvent show decrease in an intensity. Conversely the broad and intense absorption centered at 1662 cm^{-1} is transformed to a narrow intense components centered at 1667cm^{-1} with a shoulder at 1712 cm^{-1}. This latter component can be assigned to the ν(C=O) mode of the residual DMF.

Degassing at high temperature (300°C for 30 min) give rise to the spectrum presented by blue curve in Figure 5. The spectrum shows the absence of all the bands associated to the DMF and water and also the newly appeared 3676 cm^{-1} component associated to the μ_3-OH present at the Zr_6-octahedron is almost disappeared. This indicates the complete de-solvation and also de-hydroxylation of the UiO-67 framework.

3.3. Electronic properties of UiO-67: DR-UV-vis-NIR vs. theoretical calculations

3.3.1. DR-UV-vis-NIR spectroscopy. The overall electronic properties of MOFs are basically characterized by metal clusters or metal ion (mainly transition metal containing) and by organic linker, which are the main framework constituent.[64,109] The immensely available choice of framework constituent and the presence of these framework constituent with retaining their molecular properties enables to modulate not only the topological properties but also the electronic properties of the framework. For example, increase in conjugation of organic linker or using electron donor substituted arene[91] will give bathochromic shift in absorption maxima. This phenomenon is well illustrated in the UV-Vis spectra reported in Figure 6 for a series of isostructural UiOs-66/67. In accordance to what has been observed for UiO-66,[64] we anticipate that the band gap in UiO-67 is defined by the linker.

Figure 6a shows the DRS UV-Vis spectra of UiO-67 (hydroxylated, cyan curve, and dehydroxylated, blue curve) and its comparison with monocline ZrO_2 (gray curve). Figure 6b reports the DRS UV-Vis spectra of UiO-66 (orange curve) and UiO-66-NH_2 (pink curve), while the spectrum of UiO-67 is repeated for a direct comparison. The spectra of the hydroxylated and dehydroxylated forms of UiO-67 show an absorption edge around 337 and 354 nm respectively (3.66 and 350 eV) ascribed to the $\pi \rightarrow \pi*$ electronic transition of the biphenyl linker system. The absorption edge going from the hydroxylated to the dehydroxylated firm of UiO-67 is blue shifted, as previously observed for UiO-66.[64] The red shift of the UiO-66 band gap with respect to the $\pi \rightarrow \pi^*$ transitions of benzene, is a consequence of the conjugation with the two carboxylate groups. A further conjugation in biphenyl linker further reduces the energy gap (E_g) moving from UiO-66 to UiO-67; 305 nm (4.07 eV) *vs.* 337 nm (3.66 eV), see Figure 6b.

The role of organic linker in defining the band gap of UiOs framework was well utilized by Silva et al.,[87] demonstrating the enhanced photocatalytic activity of UiO-66-NH_2 over UiO-66 in the production of hydrogen from methanol/water system. The enhanced activity was obtained by increase in the light absorption by the presence of-NH_2 group in linker. The spectrum of UiO-66-NH_2 as made, is shown as pink curve in Figure 6b, in this case the absorption edge is centered

around 420 nm (2.95 eV), which is responsible for the yellow color of the sample. The grafting of $Cr(CO)_3$ on the benzene rings of the BDC linker causes a only small shift of the $\pi \rightarrow \pi^*$ transition, while the band at higher wavelength is due to a $Cr(CO)_3 \rightarrow$arene charge transfer (CT). Therefore the experimental band gap order for isostructural UiOs follows : UiO-66 ≤ UiO-66-$Cr(CO)_3$ < UiO-67 < UiO-66-NH_2, see Table 5.

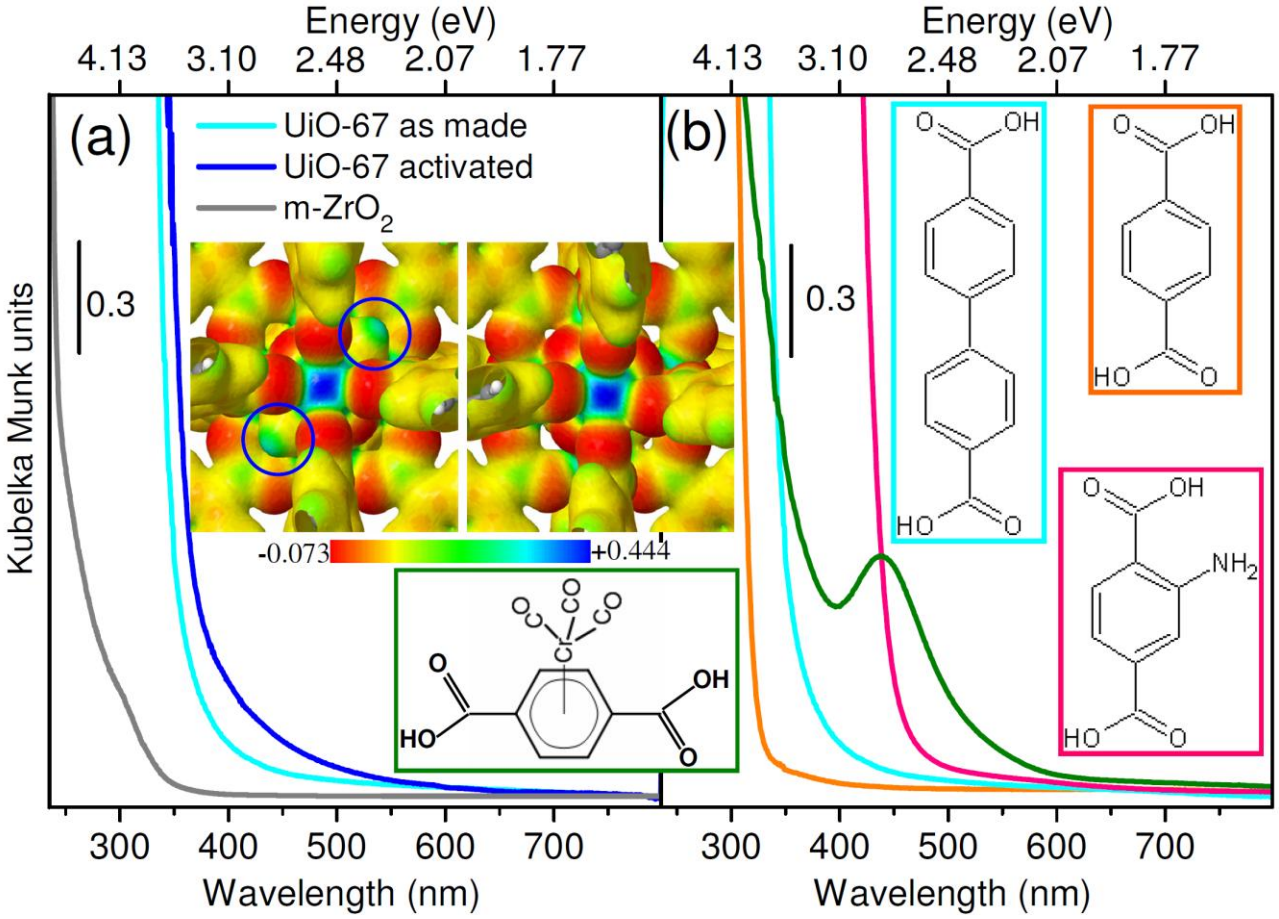

Figure 6. Part (a): DRS-UV-Vis spectra of UiO-67 in its hydroxylated (cyan curves) and dehydroxylated (blue curve) forms. For comparison, also the spectrum of monoclinic ZrO_2 is reported. The inset reports in |e|/Bohr^3 the electrostatic potential computed by CRYSTAL code at B3LYP level of theory on both hydroxylated (left) and dehydroxylated (right) forms of UiO-67. The picture is focused on the Zr_6 octahedron. In both parts, the positive potential of the Zr atoms is clearly visible, as well as the four coordinated, negatively charged, oxygen of the carboxylate units. μ_3-OH units are evidenced by blue circles in the left part. Part (b): modification of the energy gap of the UiO-66-67 family upon change of ligand (all hydroxylated forms but UiO-66-$Cr(CO)_3$). The rectangles report in the same color code as the spectra the different linkers used to form UiO-67 (cyan), UiO-66 (orange), UiO-66-NH_2 (pink) and UiO-66-$Cr(CO)_3$ (green).

Table 5. Band gaps (in eV) for the hydroxylated and dehydroxylated forms of UiO-67 and UiO-66 and for UiO-66-NH_2 and UiO-66-$Cr(CO)_3$ functionalized MOFs.

System	Experimental	Calculated	Assignment	Ref
UiO-66 hydroxylated	4.07[a]	4.56[a]	$\pi \rightarrow \pi^*$	[64]
UiO-66 dehydroxylated	3.94[a]	4.19[a]	$\pi \rightarrow \pi^*$	[64]
UiO-67 hydroxylated	3.68	4.06[a]	$\pi \rightarrow \pi^*$	This work
UiO-67 dehydroxylated	3.50	3.97[a]	$\pi \rightarrow \pi^*$	This work
UiO-66-NH_2 hydroxylated	2.95	-	$\pi \rightarrow \pi^*$	This work
UiO-66-$Cr(CO)_3$ dehydroxylated	3.72	4.35[b]	$\pi \rightarrow \pi^*$	[91]
UiO-66-$Cr(CO)_3$ dehydroxylated	2.85	2.89[b]	$Cr(CO)_3 \rightarrow$arene CT	[91]

[a] Periodic calculations performed with CRYSTAL code at B3LYP level of theory.
[b] Cluster calculations on the [η^6-$C_6H_4(COOH)_2$]$Cr(CO)_3$ molecule performed with Gaussian 03 at the B3LYP level of theory.

3.3.2. Band gap calculations.. In a previous work[64] the accuracy of the computational approach to evaluate E_g was first checked for the three forms of ZrO_2, to verify the validity of the adopted level of theory. In agreement with the results of Kralik et al.,[113] who adopted a plane wave approach, we found that the zirconia E_g increases in the order monoclinic < cubic < tetragonal.[64] Comparison with the experimental E_g value for the monoclinic phase results in an overestimation of about 22 % confirming the general overestimation of E_g computed at B3LYP level of theory.[114,115]

The systematic overestimation of the E_g computed at B3LYP level of theory is confirmed for UiO-66 and UiO-67 MOFs, see Table 5. Of interest is that computed E_g values reproduce all the experimental trends: (i) for both UiO-66 and UiO-67, computed E_g are larger in the hydroxylated forms then in the dehydroxylated ones; (ii) the experimental trend for the $\pi \rightarrow \pi^*$ transitions UiO-66 $\leq$ UiO-66-$Cr(CO)_3$ < UiO-67 < UiO-66-NH_2 is fully confirmed see Table 5.

For both UiO-66 and UiO-67, the analysis of the density of states projected on the different atoms of the framework (not reported) allows to understand the origin of the band gap tuning upon dehydroxylation. In both hydroxylated and dehydroxylated cases, the carbon atoms of the organic linker are those involved in the modulation of the band gaps while Zr atoms do not play any role. This result is similar to that obtained for MOF-5 structure.[109]

Interestingly, the E_g of UiO-67, UiO-66 and MOF-5 show different behaviour with respect to that of their corresponding oxides (i.e. ZrO_2 and ZnO). For MOF-5, the presence of valence electronic bands in the gap due to the organic linkers leads to an increase of the computed E_g (from 3.4 eV for ZnO to 5.0 eV) while, for UiO-67 (or UiO-66) this causes an E_g reduction: from 6.3 to 3.68 eV (4.07 eV). Consequently, the role of the organic linker to define the band gap of the MOF suggests that its functionalization[65,87,91] and/or interaction with adsorbed molecules are a mean to tune MOF's band gaps, opening a way for optical and sensoring applications.

The electrostatic potential was calculated and mapped on a charge density iso-surface of 0.003 |e|. 3D maps are reported in the right insert of Figure 6a; left and right parts for the hydroxylated and dehydroxylated UiO-67 structures, respectively. Red, green and blue regions represent negative, zero and positive values, respectively. In the right part, a prominent neutral zone shows up corresponding to the hydrogen atom of the μ3-OH units in the inorganic brick of the hydroxylated system (evidenced by the blue circles). In both parts, the positive areas around the zirconium atom (blue spots) are very similar, while the negative zone in looks stronger in the hydroxylated form. Comparison between the two parts allows to have a qualitative view on the electronic rearrangement undergone by the $Zr_6O_4(OH)_4$ unit upon dehydroxylation. On top of this, such qualitative pictures can be of help in the identification of preferential adsorption sites for small molecules; nevertheless, in the present case, the high packing of the $Zr_6O_4(OH)_4$ and Zr_6O_7 units (that are linked to twelve BPDC units) do not allow access to the metal centers. Molecular adsorption, even for H_2 is then expected to occur mainly on the BPDC linkers. This aspect, suggested by calculations will be confirmed by temperature dependent IR spectroscopy of adsorbed H_2, see Section 3.4.2.

3.4. H_2 adsorption onto UiO-67: comparison with UiO-66

3.4.1. Volumetric Measurements. The H_2 isotherm obtained at 77 K on UiO-67 is reported in Figure 7 (blue symbols) and compared to that collected on UiO-66 (red symbols). For both materials. the fully reversibility of the adsorption process is evident from the complete coincidence of the adsorption and desorption curves. The equilibrium for each point was reached after less than 100 s indication of the unhindered diffusion of H_2 inside the pores of the material. In all the cases the excess mass% reached its maximum at pressure definitely lower than *P*=80 bar, in particular: 2.4 mass% at 31 bar for UiO-66 (2.2 mass% at 84 bar) and 4.6 mass% at 38 bar for UiO-67 (4.2 mass% at 81 bar).

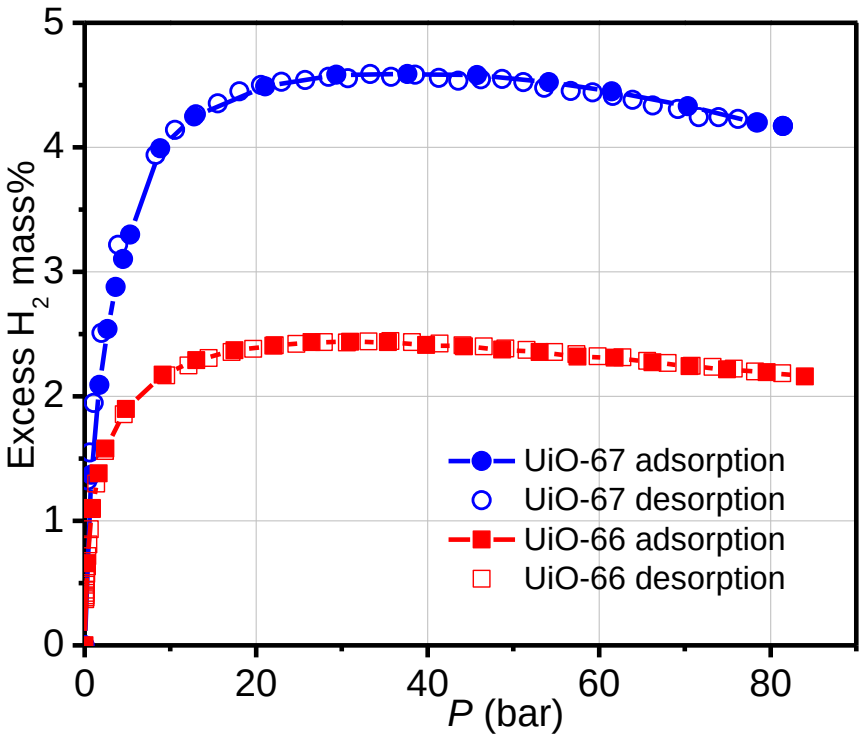

Figure 7. H_2 excess isotherms recorded at 77 K on UiO-66 (red squares) and UiO-67 (blue circles). Full and open symbols refer to the adsorption and desorption branches, respectively.

The H_2 uptakes have a linear dependence on the surface area and pore volume at high pressure as expected on qualitative speculations and on previous results reported in literature. The values obtained are close to those expected on the basis of the surface area and with the hypothesis of monolayer formation (having the same hydrogen density at the triple point (0.077 g cm^{-3}). This result indicates the samples were fully activated. This also indicates that, in the present cases, the growth of both UiO-66 and UiO-67 didn't suffers of co-penetration problems observed in other cases.[29] An uptake of 4.6 mass% at 38 bar, although noteworthy being among the highest vales reported so far, it is sensitively lower than those reported for MIL-101, IRMOF-20 and MOF-177 in the same pressure and temperature conditions (6.1, 6.2 and 7.0 mass%, respectively).[44,116] Nevertheless the great chemical and thermal stability of UiO-67 and the absence of Cr in its structure would make this material competitive with respect to the other MOFs, although the temperature and pressure conditions of storage make its use as material for H_2 storage not economically sustainable.

3.4.2. Variable Temperature FTIR spectroscopy. The IR spectra recorded for the adsorption of H_2 on isoreticular UiO MOFs as a function temperature (15-300 K) with initial pressure of 45-50 mbar of H_2 are reported in Figure 8. In all the cases, the first IR signal of adsorbed hydrogen was observed in the temperature (T_{onset}) range of 100 – 95 K. This T_{onset} value is similar to the one found for the MOFs without accessible metal sites (such as MOF-5)[47] and for organic polymers (polystyrene).[117] This T_{onset} value is quite lower with respect to MOFs with accessible metal sites such as HKUST-1 (140 K) and CPO-27-Ni (180 K).[47] The IR spectra of hydrogen adsorbed on hydroxylated (solvent removed) and dehydroxylated UiO-67 (Figure 8a, b respectively) have a complex structure, where different peaks corresponds to hydrogen interacting with different adsorption sites. For comparison, Figure 8c shows the IR spectra obtained for the hydrogen adsorption on dehydroxylated UiO-66.

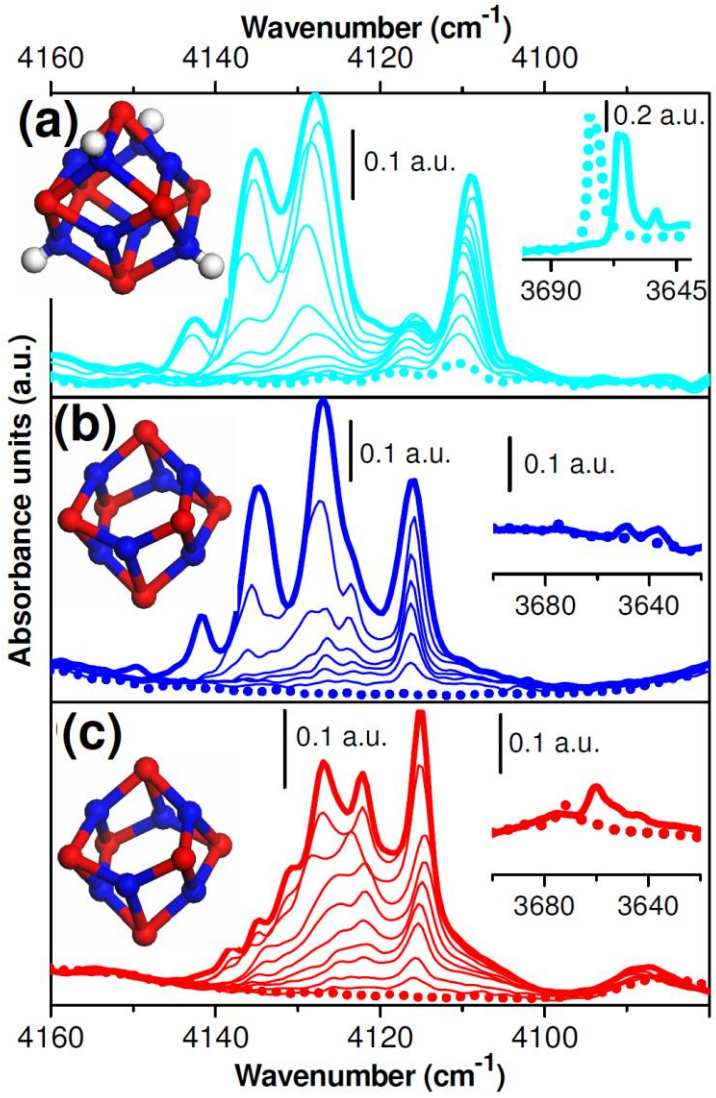

Figure 8. FTIR spectra of H_2 adsorbed on hydroxylated UiO-67, dehydroxylated UiO-67 and dehydroxylated UiO-66 as a function of temperature (100-15K): parts (a), (b) and (c), respectively. Dotted curves represent the activated material before H_2 dosage (spectra collected at 15 K). Bold curves represent the highest H_2 coverage (spectra collected at 15 K). Intermediate curves, from bold to dotted curve represents spectra collected at increasing temperatures. Right insets show the ν(OH) stretching region of the IR spectra before (dotted curves) and after (bold curves) H_2 dosage. Left insets show the structure of the $Zr_6O_4(OH)_4$ and Zr_6O_6 octahedra acting as inorganic cornerstones for the hydroxylated and dehydroxylated forms of the UiO-66/67 family.

The adsorption of H_2 to the surface site of any nature (cationic or anionic) perturbs the molecule causing the appearance of an induced dipole that makes active band due to ν(H-H) stretching mode. This results in the appearance in the IR spectra of ν(H-H) bands red shifted from the gas phase Raman value (4160 cm^{-1}), being both the red shift and the extinction coefficient correlated to the perturbation induced by the adsorbing site on the molecule.[66,67,69] In all the three cases investigated in Figure 8 the most perturbed vibration band is observed at 4108 cm^{-1} (Δν(H-H) -52 cm^{-1}). This band is assigned to the ν(H-H) of the hydrogen in an interaction with μ3-OH hydroxyl groups of the $Zr_6O_4(OH)_4$ inorganic cornerstones. This is evident from the simultaneous changes in the OH region: erosion of a band, 3677 cm^{-1} of μ3-OH hydroxyl group with the formation of a new band at 3668 cm^{-1} as shown in the right insets. In case of dehydroxylated UiO-67 and UiO-66, the 4108 cm^{-1} component appear very weak, consistent to almost complete removal of these species (right inset of Figure 8b,c). A second most red shifted (Δν(H-H) = -44 cm^{-1}) hydrogen vibration is observed at 4116 cm^{-1} which appears as medium intense in the hydroxylated

form of UiO-67 while is the main component in the dehydroxylated forms of both UiO-67 and UiO-66 materials. The intensity of this band shows inverse relation with highly perturbed band at 4108 cm^{-1} and so with the concentration of μ3-OH hydroxyl groups, therefore the site giving rise to 4116 cm^{-1} band must be originated at the expense of hydroxyl group removal. The dehydroxylation of UiOs metal organic framework is depicted in the left insets of Figure 8a,b. The four hydroxyl groups from a $Zr_6O_4(OH)_4$ cluster are released in the form of two water molecule generating triply bridged μ3-O species at the cluster surface.

Therefore, we assign the 4116 cm^{-1} component to the hydrogen interacting with μ_3-O sites. Upon further lowering the temperature (so increasing in coverage) the bands at 4108 and 4116 cm^{-1} show increase in intensity with simultaneous growth of number of peaks in 4120- 4145 cm^{-1} region. The bands in the 4120-4145 cm^{-1} region in both UiO-66 and UiO-67 are due to H_2 interacting with organic linker and to hydrogen molecules condensed inside pores. These results shows that hydrogen is more perturbed upon interaction with surface hydroxyl groups than that upon interaction with surface triply briged "oxo" species. Moreover, obtaining hydroxylated MOF is less energy demanding than obtaining completely dehydroxylated, suggesting that .the ideal activation of UiO-66/67 MOFs family for H_2 storage is 250 °C, where DMF has already leaved the material, being the inorganic cornerstones still in their hydroxylated form.

4. Conclusions

In this work we report the first complete structural, vibrational and electronic characterization of the UiO-67 MOF, isostructural to UiO-66, obtained using the longer BPDC linker in stead of BDC. Periodic calculations performed at B3LYP level of theory allow a straightforward assignment of the experimental data.

XRPD, TG proved the thermal stability of UiO-67 to be as high as that of UiO-66 material (450 °C). Zr K-edge EXAFS testifies that the inorganic cornerstones of UiO-67 is the same Zr_6 octahedron as for UiO-66, just slightly modified by the change of ligands. The optimized structures at B3LYP level confirm this observation. Calculations also allow obtaining a full understanding of the vibrational (ATR IR) and electronic (DRS UV-Vis) properties of UiO-67. In particular, the experimental trend for the $\pi \rightarrow \pi^*$ transitions UiO-66 ≤ UiO-66-$Cr(CO)_3$ < UiO-67 < UiO-66-NH_2 is fully confirmed by periodic calculation, demonstrating the role of the organic linker to define the band gap of the MOF and suggesting that MOFs functionalization[65,87,91] and/or interaction with adsorbed molecules are a mean to tune MOF's band gaps, opening a way for optical and sensoring applications.

Both UiO-66 and UiO-67 materials have been tested for molecular hydrogen storage at high pressures and at liquid nitrogen temperature. In this regard, the use of a longer ligand has a double benefit as (i) it reduces the density of the material and (ii) it increases the Langmuir surface area from 1281 to 2483 $m^2\ g^{-1}$ and the micropore volume from 0.43 to 0.85 $cm^3\ g^{-1}$. As a consequence, the H_2 uptake at 38 bar and 77 K increases from 2.4 mass% for UiO-66 up to 4.6 mass% for the new UiO-67 material. This value is among the highest vales reported so far but is lower than those reported for MIL-101, IRMOF-20 and MOF-177 in similar pressure and temperature conditions (6.1, 6.2 and 7.0 mass%, respectively).[44,116] Nevertheless the great chemical and thermal stability of UiO-67 and the absence of Cr in its structure would make this material competitive.

Temperature dependent (in the 15-300 K range) IR experiments allows to understand the nature of the interaction between H_2 molecule and the internal surfaces of UiO-66 and UiO-67 MOFs. These experiments showed that, due to a specific interaction between H_2 and μ3-OH group of the $Zr_6O_4(OH)_4$ inorganic cornerstones, the most suitable forms of both UiO-66 and UiO-67 for H_2 storage is the hydroxylated one. Consequently the best activation temperature of these materials for this purpose is 250 °C, allowing DMF removal, without dehydroxylation of the inorganic cornerstones.

Acknowledgements

The authors thank: (i) the staffs of BM29 (in particular C. Prestipino) and of BM01 (SNBL, in particular H. Emerich) beamlines at the ESRF, Grenoble, France for the EXAFS data collection on UiO-66 and UiO-67, respectively; (ii) Dr. D. Wragg (University of Oslo) for fruitful discussion and Dr. E. Groppo (University of Turin) for having installed and made operative the ATR instrument inside the glove box; (iii) FUNMAT@UIO, inGAP, VISTA and The Research Council of Norway for the financial support.

Figure for the Table of Contents

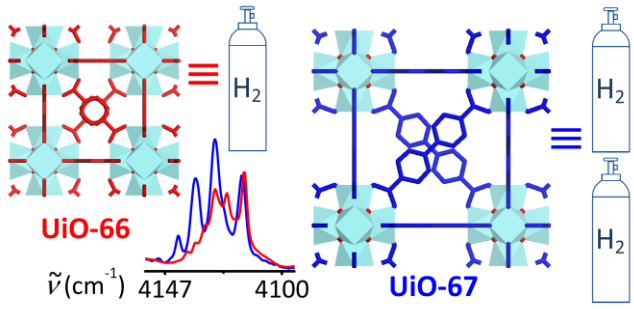

Short text for the Table of Contents

Increasing the length of the organic linker, from BDC of UiO-66 to BPDC of UiO-67, doubles the H_2 uptake of the MOF.

References

1 A. K. Cheetham, G. Ferey and T. Loiseau, *Angew. Chem.-Int. Edit.*, 1999, **38**, 3268.
2 M. Eddaoudi, D. B. Moler, H. L. Li, B. L. Chen, T. M. Reineke, M. O'Keeffe and O. M. Yaghi, *Accounts Chem. Res.*, 2001, **34**, 319.
3 S. L. James, *Chem. Soc. Rev.*, 2003, **32**, 276.
4 D. Bradshaw, J. B. Claridge, E. J. Cussen, T. J. Prior and M. J. Rosseinsky, *Accounts Chem. Res.*, 2005, **38**, 273.
5 G. Ferey, *Chem. Soc. Rev.*, 2008, **37**, 191.
6 M. O'Keeffe, *Chem. Soc. Rev.*, 2009, **38**, 1215.
7 J. J. Perry IV, J. A. Perman and M. J. Zaworotko, *Chem. Soc. Rev.*, 2009, **38**, 1400.
8 D. J. Tranchemontagne, J. L. Mendoza-Cortes, M. O'Keeffe and O. M. Yaghi, *Chem. Soc. Rev.*, 2009, **38**, 1257.
9 J. R. Long and O. M. Yaghi, *Chem. Soc. Rev.*, 2009, **38**, 1213.
10 S. S. Han, J. L. Mendoza-Cortes and W. A. Goddard, *Chem. Soc. Rev.*, 2009, **38**, 1460.
11 J. Lee, O. K. Farha, J. Roberts, K. A. Scheidt, S. T. Nguyen and J. T. Hupp, *Chem. Soc. Rev.*, 2009, **38**, 1450.
12 D. Farrusseng, S. Aguado and C. Pinel, *Angew. Chem.-Int. Edit.*, 2009, **48**, 7502.
13 O. K. Farha and J. T. Hupp, *Accounts Chem. Res.*, 2010, **43**, 1166.
14 S. Bordiga, F. Bonino, K. P. Lillerud and C. Lamberti, *Chem. Soc. Rev.*, 2010, **39**, 4885.
15 S. Keskin and D. S. Sholl, *Energy Environ. Sci.*, 2010, **3**, 343.
16 A. Corma, H. Garcia and F. X. L. Xamena, *Chem. Rev.*, 2010, **110**, 4606.
17 M. Ranocchiari and J. A. van Bokhoven, *Phys. Chem. Chem. Phys.*, 2011, **13**, 6388.
18 D. Zhao, D. J. Timmons, D. Q. Yuan and H. C. Zhou, *Accounts Chem. Res.*, 2011, **44**, 123.
19 G. Ferey, C. Serre, T. Devic, G. Maurin, H. Jobic, P. L. Llewellyn, G. De Weireld, A. Vimont, M. Daturi and J. S. Chang, *Chem. Soc. Rev.*, 2011, **40**, 550.
20 A. Nalaparaju, X. S. Zhao and J. W. Jiang, *Energy Environ. Sci.*, 2011, **4**, 2107.
21 J. M. Simmons, H. Wu, W. Zhou and T. Yildirim, *Energy Environ. Sci.*, 2011, **4**, 2177.
22 U. Müller, M. Schubert, F. Teich, H. Puetter, K. Schierle-Arndt and J. Pastre, *J. Mater. Chem.*, 2006, **16**, 626.
23 A. Czaja, T. Trukhan and U. Müller, *Chem. Soc. Rev.*, 2009, **38**, 1284.
24 H. Li, M. Eddaoudi, M. O'Keeffe and O. M. Yaghi, *Nature*, 1999, **402**, 276.
25 S. S. Y. Chui, S. M. F. Lo, J. P. H. Charmant, A. G. Orpen and I. D. Williams, *Science*, 1999, **283**, 1148.
26 N. L. Rosi, M. Eddaoudi, J. Kim, M. O'Keeffe and O. M. Yaghi, *Crystengcomm*, 2002, 401.
27 K. C. Szeto, K. P. Lillerud, M. Tilset, M. Bjorgen, C. Prestipino, A. Zecchina, C. Lamberti and S. Bordiga, *J. Phys. Chem. B*, 2006, **110**, 21509.
28 K. C. Szeto, C. Prestipino, C. Lamberti, A. Zecchina, S. Bordiga, M. Bjorgen, M. Tilset and K. P. Lillerud, *Chem. Mater.*, 2007, **19**, 211.
29 J. Hafizovic, M. Bjorgen, U. Olsbye, P. D. C. Dietzel, S. Bordiga, C. Prestipino, C. Lamberti and K. P. Lillerud, *J. Am. Chem. Soc.*, 2007, **129**, 3612.
30 J. H. Cavka, S. Jakobsen, U. Olsbye, N. Guillou, C. Lamberti, S. Bordiga and K. P. Lillerud, *J. Am. Chem. Soc.*, 2008, **130**, 13850.
31 J. Perles, N. Snejko, M. Iglesias and M. A. Monge, *J. Mater. Chem.*, 2009, **19**, 6504.
32 K. C. Stylianou, R. Heck, S. Y. Chong, J. Bacsa, J. T. A. Jones, Y. Z. Khimyak, D. Bradshaw and M. J. Rosseinsky, *J. Am. Chem. Soc.*, 2010, **132**, 4119.
33 S. Motoyama, R. Makiura, O. Sakata and H. Kitagawa, *J. Am. Chem. Soc.*, 2011, **133**, 5640.

34 I. J. Kang, N. A. Khan, E. Haque and S. H. Jhung, *Chem.-Eur. J.*, 2011, **17**, 6437.
35 V. Colombo, S. Galli, H. J. Choi, G. D. Han, A. Maspero, G. Palmisano, N. Masciocchi and J. R. Long, *Chem. Sci.*, 2011, **2**, 1311.
36 H. Furukawa, N. Ko, Y. B. Go, N. Aratani, S. B. Choi, E. Choi, A. O. Yazaydin, R. Q. Snurr, M. O'Keeffe, J. Kim and O. M. Yaghi, *Science*, 2010, **329**, 424.
37 N. L. Rosi, J. Eckert, M. Eddaoudi, D. T. Vodak, J. Kim, M. O'Keeffe and O. M. Yaghi, *Science*, 2003, **300**, 1127.
38 J. L. C. Rowsell, A. R. Millward, K. S. Park and O. M. Yaghi, *J. Am. Chem. Soc.*, 2004, **126**, 5666.
39 J. L. C. Rowsell, E. C. Spencer, J. Eckert, J. A. K. Howard and O. M. Yaghi, *Science*, 2005, **309**, 1350.
40 M. Dinca and J. R. Long, *J. Am. Chem. Soc.*, 2005, **127**, 9376.
41 M. Dinca, A. Dailly, Y. Liu, C. M. Brown, D. A. Neumann and J. R. Long, *J. Am. Chem. Soc.*, 2006, **128**, 16876.
42 D. F. Sun, S. Q. Ma, Y. X. Ke, D. J. Collins and H. C. Zhou, *J. Am. Chem. Soc.*, 2006, **128**, 3896.
43 P. M. Forster, J. Eckert, B. D. Heiken, J. B. Parise, J. W. Yoon, S. H. Jhung, J. S. Chang and A. K. Cheetham, *J. Am. Chem. Soc.*, 2006, **128**, 16846.
44 A. G. Wong-Foy, A. J. Matzger and O. M. Yaghi, *J. Am. Chem. Soc.*, 2006, **128**, 3494.
45 Y. W. Li and R. T. Yang, *J. Am. Chem. Soc.*, 2006, **128**, 726.
46 S. Bordiga, L. Regli, F. Bonino, E. Groppo, C. Lamberti, B. Xiao, P. S. Wheatley, R. E. Morris and A. Zecchina, *Phys. Chem. Chem. Phys.*, 2007, **9**, 2676.
47 J. G. Vitillo, L. Regli, S. Chavan, G. Ricchiardi, G. Spoto, P. D. C. Dietzel, S. Bordiga and A. Zecchina, *J. Am. Chem. Soc.*, 2008, **130**, 8386.
48 (*a*) D. Zhao, D. Q. Yuan and H. C. Zhou, *Energy Environ. Sci.*, 2008, **1**, 222. (*b*) J. Sculley, D. Q. Yuan and H. C. Zhou, *Energy Environ. Sci.*, 2011, **4**, 2721.
49 L. F. Wang and R. T. Yang, *Energy Environ. Sci.*, 2008, **1**, 268.
50 L. J. Murray, M. Dinca and J. R. Long, *Chem. Soc. Rev.*, 2009, **38**, 1294.
51 J. R. Li, R. J. Kuppler and H. C. Zhou, *Chem. Soc. Rev.*, 2009, **38**, 1477.
52 Y. H. Hu and L. Zhang, *Adv. Mater.*, 2010, **22**, E117.
53 K. Sumida, S. Horike, S. S. Kaye, Z. R. Herm, W. L. Queen, C. M. Brown, F. Grandjean, G. J. Long, A. Dailly and J. R. Long, *Chem. Sci.*, 2010, **1**, 184.
54 H. J. Choi, M. Dinca, A. Dailly and J. R. Long, *Energy Environ. Sci.*, 2010, **3**, 117.
55 Z. H. Xiang, D. P. Cao, J. H. Lan, W. C. Wang and D. P. Broom, *Energy Environ. Sci.*, 2010, **3**, 1469.
56 R. E. Hester, R. M. Harrison, J. C. Kuylenstierna, W. K. Hicks and M. J. Cahdwick, *A perspective on global air pollution problems*, in: Global Environmental Change; R. E. Hester and R. M. Harrison, Ed.; The Royal Society of Chemistry: Cambridge, **2002**, p. 21.
57 D. A. J. Rand and R. M. Dell, *Hydrogen Energy: Challenges and Prospects*; The Royal Society of Chemistry: Cambridge, **2008**.
58 M. Z. Jacobson, *Energy Environ. Sci.*, 2009, **2**, 148.
59 U. Eberle and R. von Helmolt, *Energy Environ. Sci.*, 2010, **3**, 689.
60 C. Weidenthaler and M. Felderhoff, *Energy Environ. Sci.*, 2011, **4**, 2495.
61 K. M. Thomas, *Dalton Trans.*, 2009, 1487.
62 G. Ferey, *J. Solid State Chem.*, 2000, **152**, 37.
63 S. S. Han, H. Furukawa, O. M. Yaghi and W. A. Goddard, *J. Am. Chem. Soc.*, 2008, **130**, 11580.
64 L. Valenzano, B. Civalleri, S. Bordiga, M. H. Nilsen, S. Jakobsen, K.-P. Lillerud and C. Lamberti, *Chem. Mater.*, 2011, **23**, 1700–1718.
65 M. Kandiah, S. Usseglio, S. Svelle, U. Olsbye, K. P. Lillerud and M. Tilset, *J. Mater. Chem.*, 2010, **20**, 9848.
66 E. N. Gribov, S. Bertarione, D. Scarano, C. Lamberti, G. Spoto and A. Zecchina, *J. Phys. Chem. B*, 2004, **108**, 16174.
67 G. Spoto, E. Gribov, S. Bordiga, C. Lamberti, G. Ricchiardi, D. Scarano and A. Zecchina, *Chem. Commun.*, 2004, 2768.
68 G. Spoto, S. Bordiga, A. Zecchina, D. Cocina, E. N. Gribov, L. Regli, E. Groppo and C. Lamberti, *Catal. Today*, 2006, **113**, 65.
69 C. Lamberti, A. Zecchina, E. Groppo and S. Bordiga, *Chem. Soc. Rev.*, 2010, **39**, 4951.
70 A. D. Becke, *J. Chem. Phys.*, 1993, **98**, 5648.
71 C. Lee, W. Yang and R. G. Parr, *Phys. Rev. B*, 1988, **37**, 785.
72 R. Dovesi, R. Orlando, B. Civalleri, C. Roetti, V. R. Saunders and C. M. Zicovich-Wilson, *Z. Kristallogr.*, 2005, **220**, 571.
73 R. Dovesi, V. R. Saunders, R. Roetti, R. Orlando, C. M. Zicovich-Wilson, F. Pascale, B. Civalleri, K. Doll, N. M. Harrison, I. J. Bush, P. D'Arco and M. Llunell, *CRYSTAL09, University of Torino, Torino*, 2009.
74 L. Valenzano, B. Civalleri, S. Chavan, G. T. Palomino, C. O. Arean and S. Bordiga, *J. Phys. Chem. C*, 2010, **114**, 11185–11191.
75 G. Spoto, E. N. Gribov, G. Ricchiardi, A. Damin, D. Scarano, S. Bordiga, C. Lamberti and A. Zecchina, *Prog. Surf. Sci.*, 2004, **76**, 71.
76 C. Lamberti, C. Prestipino, S. Bordiga, G. Berlier, G. Spoto, A. Zecchina, A. Laloni, F. La Manna, F. D'Anca, R. Felici, F. D'Acapito and P. Roy, *Nucl. Instrum. Meth. B*, 2003, **200**, 196.

77 B. Ravel and M. Newville, *J. Synchrot. Radiat.*, 2005, **12**, 537.
78 C. Lamberti, S. Bordiga, D. Arduino, A. Zecchina, F. Geobaldo, G. Spano, F. Genoni, G. Petrini, A. Carati, F. Villain and G. Vlaic, *J. Phys. Chem. B*, 1998, **102**, 6382.
79 S. I. Zabinsky, J. J. Rehr, A. Ankudinov, R. C. Albers and M. J. Eller, *Phys. Rev. B*, 1995, **52**, 2995.
80 The Zr basis set used in the calculation has been included in the SI within the CRYSTAL input files, alternatively see http://www.crystal.unito.it/Basis_Sets/zirconium.html#Zr_all_electron_dovesi_unpub .
81 Y. Noel, C. M. Zicovich-Wilson, B. Civalleri, P. D'Arco and R. Dovesi, *Phys. Rev. B*, 2002, **65**, Art. n. 014111.
82 C. G. Broyden, *Math. Comput.*, 1965, **19**, 577.
83 D. D. Johnson, *Phys. Rev. B*, 1988, **38**, 12807.
84 K. Doll, *Comput. Phys. Commun.*, 2001, **137**, 74.
85 K. Doll, V. R. Saunders and N. M. Harrison, *Int. J. Quantum Chem.*, 2001, **82**, 1.
86 F. Pascale, C. M. Zicovich-Wilson, F. López Gejo, B. Civalleri, R. Orlando and R. Dovesi, *J. Comput. Chem.*, 2004, **25**, 888
87 C. G. Silva, I. Luz, F. X. Llabres i Xamena, A. Corma and H. Garcia, *Chem.-Eur. J.*, 2010, **16**, 11133.
88 S. J. Garibay and S. M. Cohen, *Chem. Commun.*, 2010, **46**, 7700.
89 V. Guillerm, S. Gross, C. Serre, T. Devic, M. Bauer and G. Ferey, *Chem. Commun.*, 2010, **46**, 767.
90 K. P. Lillerud, U. Olsbye and M. Tilset, *Top. Catal.*, 2010, **53**, 859.
91 S. Chavan, J. G. Vitillo, M. J. Uddin, F. Bonino, C. Lamberti, E. Groppo, K. P. Lillerud and S. Bordiga, *Chem. Mater.*, 2010, **22**, 4602.
92 S. Gross and M. Bauer, *Adv. Funct. Mater.*, 2010, **20**, 4026.
93 M. Kandiah, M. H. Nilsen, S. Usseglio, S. Jakobsen, U. Olsbye, M. Tilset, C. Larabi, E. A. Quadrelli, F. Bonino and K. P. Lillerud, *Chem. Mat.*, 2011, **22**, 6632.
94 F. Vermoortele, R. Ameloot, A. Vimont, C. Serre and D. De Vos, *Chem. Commun.*, 2011, **47**, 1521.
95 C. Zlotea, D. Phanon, M. Mazaj, D. Heurtaux, V. Guillerm, C. Serre, P. Horcajada, T. Devic, E. Magnier, F. Cuevas, G. Ferey, P. L. Llewellyn and M. Latroche, *Dalton Trans.*, 2011, **40**, 4879.
96 M. Kim, S. J. Garibay and S. M. Cohen, *Inorg. Chem.*, 2011, **50**, 729.
97 W. Morris, C. J. Doonan and O. M. Yaghi, *Inorg. Chem.*, 2011, **50**, 6853.
98 Q. Yang, H. Jobic, F. Salles, D. Kolokolov, V. Guillerm, C. Serre and G. Maurin, *Chem. – Euro J.*, 2011, **17**, 8882.
99 Q. Y. Yang, A. D. Wiersum, H. Jobic, V. Guillerm, C. Serre, P. L. Llewellyn and G. Maurin, *J. Phys. Chem. C*, 2011, **115**, 13768.
100 A. D. Wiersum, E. Soubeyrand-Lenoir, Q. Yang, B. Moulin, V. Guillerm, M. B. Yahia, S. Bourrelly, A. Vimont, S. Miller, C. Vagner, M. Daturi, C. G., C. Serre, G. Maurin and P. L. Llewellyn, *Chem. Asian J.*, 2011, DOI: 10.1002/asia.201100201.
101 A. Schaate, P. Roy, A. Godt, J. Lippke, F. Waltz, M. Wiebcke and P. Behrens, *Chem.-Eur. J.*, 2011, **17**, 6643.
102 C. Lamberti, *Surf. Sci. Rep.*, 2004, **53**, 1.
103 C. Prestipino, L. Regli, J. G. Vitillo, F. Bonino, A. Damin, C. Lamberti, A. Zecchina, P. L. Solari, K. O. Kongshaug and S. Bordiga, *Chem. Mat.*, 2006, **18**, 1337.
104 N. Masciocchi, S. Galli, V. Colombo, A. Maspero, G. Palmisano, B. Seyyedi, C. Lamberti and S. Bordiga, *J. Am. Chem. Soc.*, 2010, **132**, 7902.
105 F. Bonino, S. Chavan, J. G. Vitillo, E. Groppo, G. Agostini, C. Lamberti, P. D. C. Dietzel, C. Prestipino and S. Bordiga, *Chem. Mater.*, 2008, **20**, 4957.
106 S. Chavan, J. G. Vitillo, E. Groppo, F. Bonino, C. Lamberti, P. D. C. Dietzel and S. Bordiga, *J. Phys. Chem. C*, 2009, **113**, 3292.
107 S. Chavan, F. Bonino, J. G. Vitillo, E. Groppo, C. Lamberti, P. D. C. Dietzel, A. Zecchina and S. Bordiga, *Phys. Chem. Chem. Phys.*, 2009, **11**, 9811.
108 L. Valenzano, J. G. Vitillo, S. Chavan, B. Civalleri, F. Bonino, S. Bordiga and C. Lamberti, *Catal. Today*, 2011, in press. doi: 10.1016/j.cattod.2011.07.020.
109 B. Civalleri, F. Napoli, Y. Noel, C. Roetti and R. Dovesi, *Crystengcomm*, 2006, **8**, 364.
110 D. S. Coombes, F. Cora, C. Mellot-Draznieks and R. G. Bell, *J. Phys. Chem. C*, 2009, **113**, 544.
111 A. M. Walker, B. Civalleri, B. Slater, C. Mellot-Draznieks, F. Cora, C. M. Zicovich-Wilson, G. Roman-Perez, J. M. Soler and J. D. Gale, *Angew. Chem.-Int. Edit.*, 2010, **49**, 7501.
112 Animations of anharmonic vibrational modes of hydroxylated and dehydroxylated UiO-67 will be available after publication at the http://www.crystal.unito.it/vibs/uio66_hydro/ and http://www.crystal.unito.it/vibs/uio66_dehydro/, Web sites respectively, or from the authors upon request (bartolomeo.civalleri@unito.it).
113 B. Kralik, E. K. Chang and S. G. Louie, *Phys. Rev. B*, 1998, **57**, 7027.
114 J. Muscat, A. Wander and N. M. Harrison, *Chem. Phys. Lett.*, 2001, **342**, 397.
115 A. Damin, F. X. L. Xamena, C. Lamberti, B. Civalleri, C. M. Zicovich-Wilson and A. Zecchina, *J. Phys. Chem. B*, 2004, **108**, 1328.
116 M. Dinca and J. R. Long, *Angew. Chem.-Int. Edit.*, 2008, **47**, 6766.
117 S. Figueroa-Gerstenmaier, C. Daniel, G. Milano, G. Guerra, O. Zavorotynska, J. G. Vitillo, A. Zecchina and G. Spoto, *Phys. Chem. Chem. Phys.*, 2010, **12**, 5369.